

X-ray absorption and diffraction studies of magnetic nanoparticle assemblies

S. Anders,^{a)} M. F. Toney, T. Thomson, R. F. C. Farrow, J.-U. Thiele, and B. D. Terris

IBM Almaden Research Center, 650 Harry Road, San Jose, CA 95120

Shouheng Sun and C. B. Murray

IBM T. J. Watson Research Center, Yorktown Heights, NY 10598

^{a)} Electronic mail: simone@almaden.ibm.com

We have produced assemblies of FePt nanoparticles using high temperature solution phase synthesis and polymer-mediated layer-by-layer deposition allowing precise control of the particle self-assembly. The as-deposited particles have a narrow size distribution offering the potential for use as ultra-high density magnetic storage media and ultimately storage of one bit per individual nanoparticle. Vibrating sample magnetometry was applied to measure the magnetic properties of the particle assemblies as a function of anneal condition while Near Edge X-ray Absorption Fine Structure (NEXAFS) spectroscopy and x-ray diffraction (XRD) were used to investigate the chemical nature and structural properties. It was found that the coercivity can be as high as 22.7 kOe for samples annealed at 800°C, the moment density (normalized to the particle volume) has a maximum of 1140 emu/cm³ for annealing at 650°C equal to the value for bulk FePt. NEXAFS spectroscopy shows that the Fe in the as-deposited assemblies is partly oxidized, and the oxidation is greatly reduced by annealing. XRD indicates an increased formation of the chemically ordered, high anisotropy L1₀ phase and the onset of nanoparticle agglomeration for annealing at higher temperatures.

1. Introduction

The areal storage density of magnetic hard drives has doubled annually over the last few years and this increase requires continuous improvements of the magnetic storage media. Storage densities of > 100 Gbits/in² have been demonstrated recently [1, 2] using antiferromagnetically coupled media with an average grain diameter of about 9 nm. To achieve high densities grain sizes are expected to shrink further [3]. The thermal stability of magnetic storage media has become a major concern [4] since the energy stored per grain $K_U V$ decreases with grain volume V (K_U is the magneto-crystalline anisotropy constant). Narrow grain size distributions with small average grain diameters and high magneto-crystalline anisotropy are desirable as they lead to narrow transition widths, low noise, and enhanced thermal stability.

Magnetic FePt nanoparticle assemblies have attracted much attention recently because of their possible application as magnetic storage media [5-10] due to the fact that the chemically ordered $L1_0$ phase of FePt shows very high magnetocrystalline anisotropy up to 1×10^8 erg/cm³ [11] and the particles have a narrow size distribution with a standard deviation of $\sigma < 5\%$, and magnetic recording has been demonstrated on (relatively thick) multilayer assemblies [5]. Magnetic recording on a monolayer or very thin multilayers of self-assembled nanoparticle arrays could potentially lead to increased storage densities. Ultimately, if it was possible to obtain long range order in the particle assembly and a well-defined orientation of the easy axis of each particle it might be possible to store one bit per nanoparticle with a potential storage density of about 20 Tbits/in².

In the present paper we present Near Edge X-ray Absorption Fine Structure (NEXAFS) spectroscopy and X-ray diffraction (XRD) studies of FePt nanoparticles assemblies combined with magnetic characterization in order to optimize the deposition and anneal procedures of the films for magnetic storage applications.

2. Particle Assembly Preparation and Annealing

The FePt particles were prepared using the previously described solution phase synthesis [5, 7] combining the reduction of platinum acetylacetonate $\text{Pt}(\text{acac})_2$ and the thermal decomposition of FeCl_2 in the presence of oleic acid and oleyl amine. The precursors were added in a ratio that produces $\text{Fe}_{58}\text{Pt}_{42}$ nanoparticles which have previously been shown to exhibit the highest coercivity after annealing [5]. In order to obtain well-controlled assemblies of particles we have applied a process of polymer-mediated self-assembly [7] to form 3 layers of 4 nm diameter FePt nanoparticles on Si (111) substrates. The polymer-mediated assembly process includes the functionalization of the Si substrate by dipping it into a chloroform solution of poly(ethylenimine) (PEI), and subsequently, after rinsing and drying, immersing the substrate into a hexane dispersion of the FePt nanoparticles. Ligand exchange leads to a replacement of the stabilizing oleic acid/oleyl amine shell that surrounds the particles in the dispersion, and a strongly bound monolayer of nanoparticles is formed. The process was repeated to form 3 layers of particles. The samples were subsequently annealed in N_2 at various temperatures and durations in order to transform the particles from the as-deposited chemically disordered fcc structure to the chemically ordered L1_0 phase. FePt nanoparticles in the disordered fcc phase are superparamagnetic at room temperature

while nanoparticles in the ordered $L1_0$ phase are ferromagnetic at room temperature and exhibit high magneto-crystalline anisotropy. Annealing temperatures were 580, 650, 700, and 800°C, the annealing duration was 30 minutes for the 580°C annealing temperature and 5 minutes for all other temperatures.

3. Magnetic properties

Magnetic properties of the assemblies were measured at room temperature using vibrating sample magnetometry. The as-deposited sample is superparamagnetic at room temperature and has a low magnetic moment density of 200 emu/cm³ normalized to the particle volume assuming a packing density for the assembly of 0.13 that was estimated from high-resolution TEM images [5]. All annealed samples are ferromagnetic at room temperature and show a maximum in moment density for annealing at 650°C (Fig. 1) of 1140 emu/cm³, similar to the value for bulk FePt [11]. Very high temperature annealing at 800°C leads to reduction in moment density, however the coercivity continues to increase and reaches high values up to 22.7 kOe. The reduction in moment density is possibly caused by the onset of chemical reactions with the substrate (as discussed in Sec. 6 below). In-plane and perpendicular hysteresis loops appear similar indicating a nearly 3D randomly oriented easy axis of the particles and a low contribution of demagnetizing effects.

4. Near Edge X-ray Absorption Fine Structure (NEXAFS) spectroscopy

Near Edge X-ray Absorption Fine Structure (NEXAFS) spectroscopy at the Fe L edge was applied to study the chemical properties of the nanoparticle assemblies. The

experiments were performed at beamline 7.3.1.1. of the Advanced Light Source which is a bending magnet beamline equipped with a spherical grating monochromator providing synchrotron radiation with an energy resolution of $E/\Delta E=1800$ corresponding to an energy resolution of 0.4 eV at 700 eV. Spectra were acquired in total electron yield mode at normal incidence and the flux was normalized to the photocurrent of a gold-grid monitor. In addition we measured a number of reference samples in order to be able to identify the chemical structure of the in the nanoparticle assemblies. The reference samples included a 50 nm thin film FePt sample sputtered at room temperature from a $\text{Fe}_{50}\text{Pt}_{50}$ alloy target and capped with 2 nm Pt. Oxide reference samples were grown by oxygen-plasma-assisted molecular beam epitaxy and comprised a 51 nm thick Fe_3O_4 film grown on $\text{MgO}(001)$, a 29 nm thick $\alpha\text{-Fe}_2\text{O}_3$ film grown on $\alpha\text{-Al}_2\text{O}_3$, and a 29 nm thick $\gamma\text{-Fe}_2\text{O}_3$ film grown on $\text{MgO}(001)$. The crystalline structure of these reference samples was verified using X-ray diffraction. Details about the film growth and properties of the reference samples can be found elsewhere [12]. In addition we compared our data to reference spectra for Fe, FeO, Fe_3O_4 , $\alpha\text{-}$ and $\gamma\text{-Fe}_2\text{O}_3$ from the literature [13-23]. The iron oxides FeO (wüstite) and $\alpha\text{-Fe}_2\text{O}_3$ (hematite) are antiferromagnetic insulators with a NaCl and a corundum structure, respectively [22]. $\alpha\text{-Fe}_2\text{O}_3$ shows a Morin transition at 263K, and above this temperature it exhibits a weak ferromagnetism due to spin-canting [20]. $\gamma\text{-Fe}_2\text{O}_3$ (maghemite) and Fe_3O_4 (magnetite) are ferrimagnets with an inverse spinel structure and are an insulator and semiconductor, respectively [22].

Figure 2 shows the Fe L edge spectra of the reference samples and Figure 3 shows the spectrum of the as-deposited FePt nanoparticle assembly and the spectra of the assemblies annealed at different temperatures. The Fe in the as-deposited assembly is

clearly oxidized. Indicative of the degree of oxidation are the ratios of the peaks labeled A/B and C/D at the L_3 and L_2 edges, respectively. The C/D peak ratio normalized to the pre-edge intensity is 0.81 for α - Fe_2O_3 , 0.96 for γ - Fe_2O_3 , 1.07 for Fe_3O_4 . The as-deposited assembly has a ratio of 1.0 which is for between the values of γ - Fe_2O_3 and Fe_3O_4 . For metallic Fe there is no multiplet structure of the L_2 and L_3 edges and the peaks B and D do not exist.

With increasing annealing temperature the spectra change and can be fitted by a linear superposition of a metallic Fe and a Fe_3O_4 spectrum. In Figure 3 we see the development of the NEXAFS spectra with increasing annealing temperature with a clear increase of the A/B and C/D peak ratios indicating increased metallic iron content and chemical reduction induced by the annealing. Some fraction of the Fe remains in an oxidized state up to the highest annealing temperatures studied here. For the highest temperature of 800°C the measured spectrum can be approximated by a superposition of a Fe and a Fe_3O_4 spectrum in the ratio of about 50%/50%. The spectra can be similarly well approximated by superposition of a metallic Fe and a γ - Fe_2O_3 spectrum which results in somewhat higher metallic Fe contributions to the total spectrum (e.g., about 65%/35% for the sample annealed at 800°C). There might also be a mixture of various oxides present. However we can conclude that a significant fraction of the NEXAFS spectral intensity is due to iron oxide.

We next consider how the contribution might arise in the nanoparticle system. We can assume a particle geometry of a metallic FePt core surrounded by an iron oxide shell similar to that observed for Fe particles [24]. The number of electrons $N_{e,x}$ emitted

from a layer of material x with a thickness z_x caused by an incoming number of photons I_0 as a function of photon energy E is given by [25]

$$N_{e,x} = I_0 \frac{G_x(E)}{1 + \frac{1}{\mu_x(E)\lambda_x}} \left(1 - \exp\left(-z_x\left(\mu_x(E) + \frac{1}{\lambda_x}\right)\right) \right) \quad (1)$$

where $G_x(E)$ is the photon energy dependent number of electrons produced per absorbed photon, $1/\mu_x(E)$ is the X-ray absorption length, and λ_x is the electron escape depth for the material x. If another layer of material y is buried by layer x, a fraction of the incoming photons is absorbed in layer x and emitted electrons from layer y are absorbed in layer x as well so that the number of electrons N_{e,y_under_x} emitted from layer y buried under a layer x is

$$N_{e,y_under_x} = I_0 \exp\left(-z_x\left(\mu_x(E) + \frac{1}{\lambda_x}\right)\right) \frac{G_y(E)}{1 + \frac{1}{\mu_y(E)\lambda_y}} \left(1 - \exp\left(-z_y\left(\mu_y(E) + \frac{1}{\lambda_y}\right)\right) \right) \quad (2)$$

$$= T_x N_{e,y}$$

where T_x is a factor characterizing the absorption of photons and electrons in layer x, and the total number of emitted electrons is $N_e = N_{e,x} + T_x N_{e,y}$. This can be extended to multilayer cases. To estimate the relative contributions to the spectrum from the metallic core and the oxide shell of the nanoparticle we assume a 4 layer system of carbonaceous material / iron oxide / metallic FePt / iron oxide as shown in Figure 4. The contribution to the electron emission from the carbonaceous material does not need to be taken into account because it only adds to the background signal, but the variable thickness of the carbonaceous material as a function of radial distance r from the particle center leads to an r-dependent photon and electron absorption that needs to be considered. The total

number of electrons N_e emitted from the nanoparticle as a function of radial distance from the nanoparticle center is

$$N_e(r) = T_C(r) \left(N_{e,Ox1}(r) + T_{Ox1}(r) \left(N_{FePt}(r) + T_{FePt}(r) N_{Ox2}(r) \right) \right) \quad (3)$$

The absorption factors and electron emissions from each layer all depend on r because of the thickness variations of the different layers with r as indicated in Figure 4. We assume $G_{Ox} = G_{FePt}$, and use values from the literature for the x-ray absorption length $1/\mu_x(E)$. For carbon far above the absorption edge we assume 80 nm [26], for iron oxide and Fe metal at the L_3 absorption edge energy 17 nm [27] and 15 nm [28], respectively, and for the electron escape depth λ for carbon, iron oxide, and Fe metal values of 5 nm [26], 4.5 nm [27], and 1.5 nm [28]. Using these numbers we can integrate the r -dependent electron emission over the sample surface and calculate the relative contributions from the oxide shell and the metallic core as a function of shell thickness. The result is that a very thin shell with average thickness of only 0.3 nm encapsulating a 4 nm diameter nanoparticle would contribute 50% to the spectrum, similar to the spectra observed experimentally. This is due to the geometry and the comparatively long electron escape depth of the oxide compared to the metal. Even though the numbers for the x-ray penetration depths and electron escape depths are not very accurate since they have not been measured for the exact materials used in this study, small variations in the values do not significantly modify the conclusion that a relatively thin oxide shell contributes greatly to the total spectrum. The second layer of particles does not need to be taken into account as the electron escape depth for all materials is shorter than the thickness of one monolayer of particles. The fact that the $Fe_{58}Pt_{42}$ nanoparticles (as determined from Rutherford Backscattering Spectrometry) have the highest coercivity while for thin films the highest

coercivity is obtained for a 50%/50% ratio further support the hypothesis of a metallic Fe₅₀Pt₅₀ core surrounded by a thin iron oxide shell. This needs a citation!

5. X-ray Diffraction Studies

X-ray diffraction measurements were performed in a grazing incidence geometry at the National Synchrotron Light Source using beamline X20C. The diffracted beam was collimated using 1 milliradian Soller slits, which provided an angular resolution much higher than that required to resolve any of the diffraction peak widths. Before discussing the diffraction data, it is useful to recall some structural properties of FePt. Chemically disordered FePt forms an fcc phase, while the chemically ordered L1₀ phase is fct (face-centered tetragonal), consisting of alternating planes of Fe and Pt along the c-axis. In the L1₀ phase, superlattice diffraction peaks develop and some of the fundamental (fcc) peaks split. The extent of chemical order is given by the Warren long-range order parameter S , which is unity for complete chemical order, zero for chemical disorder, and proportional to extent of chemical order for partial order (see [29] for details). In the perfectly ordered L1₀ phase of FePt alternating layers perpendicular to the c axis are occupied by Fe and Pt atoms. The order parameter S is defined as $S = r_{\text{Fe}} + r_{\text{Pt}} - 1$ where r_{Fe} and r_{Pt} are the fraction Fe and Pt sites occupied by the right atom.

The nanoparticle assemblies (as with thin films) are inhomogeneous with chemically ordered and disordered regions. Hence, we can distinguish the order parameter inside the chemically ordered regions S , the volume fraction of the assembly that is chemically ordered f_0 , and the average chemical order $S_{\text{ave}} = S f_0$.

Figure 5 shows the X-ray scans for the unannealed sample compared to the samples annealed at different temperatures. Several trends are apparent. First, the unannealed sample forms an fcc phase, as the $L1_0$ superlattice ((001) and (110)) peaks are absent. Second, the superlattice peak intensities increase with increasing annealing temperature, which shows that the extent of chemical order increases. Third, the diffraction peaks become sharper and the $L1_0$ (220)/(202) peak splitting increases with higher temperature annealing. The peak splitting results from both the increased chemical order and the peak sharpening due to nanoparticle coalescence.

The diffraction data in Fig. 5 enable calculation of the extent of chemical order which is quantified with S_{ave} and f_0 . Figure 6 shows these results. Chemical order is established by annealing at 580° C and increases with increased annealing temperature. A high degree of chemical order is obtained at 800° C, which correlates with the highest coercivity (see Fig. 1). In parallel with the establishment of chemical order, the grain size of the FePt assemblies increases. This is also shown in Fig. 6, which plots the nanoparticle grain diameter d determined using the integral-breadth method [30]. With increasing annealing temperature, the X-ray diffraction grain diameter increases significantly from 2.5 nm to nearly 20 nm. This shows that annealing leads to coalescence of the nanoparticle assemblies. At the highest annealing temperature (required to obtain S near unity), coalescence results in an average particle diameter of nearly 20 nm, which suggests that about 25 of the initial 4 nm nanoparticles have coalesced into grains after 800° C annealing. This agglomeration probably contributes to the increased coercivity in these assemblies. The crystallographic grain diameter in the

initially deposited assemblies (2.4 nm) is less than nanoparticle diameter (4 nm) because, on average, the assemblies are not single grains.

From the X-ray diffraction data, we have determined the lattice parameters a and c of the nanoparticle assemblies. For the annealed assemblies, the lattice parameter a decreases slightly with annealing temperature (from 3.87 to 3.85 Å), while c increases slightly (from 3.71 to 3.73 Å). These values are similar to those for the L1₀ FePt films and bulk alloys [29]. Interestingly, the lattice parameter in the as-deposited assembly is 3.88 Å. This is much larger than that for fcc FePt (3.80 Å) [29] and probably results from the significant oxidation of Fe described above, which increases the Pt/Fe ratio in the particle core.

Measurements of the nanoparticle texture were made on several annealed samples. These showed that the initially deposited nanoparticles had a nearly isotropic crystallographic orientation (texture). With increased annealing temperature, some (001) texture ((001) planes preferentially aligned along the substrate) began to develop. Such a texture would be desirable from a perpendicular recording media standpoint.

6. X-ray Reflectivity

X-ray reflectivity was used to determine the electron density profiles of several of the 3 layer, 4 nm assemblies. In X-ray reflectivity, the reflected X-ray intensity is measured as a function of incidence angle and the data are analyzed using a multilayer model that incorporates several parameters which are varied to produce the best fit to the data [31]. X-ray reflectivity data are shown in Fig. 7 for the as-deposited assembly, the assemblies annealed at 580°C, and at 800°C. The reflectivity for the initially deposited

assembly has a great deal of structure, but with increased annealing temperature, this structure disappears. This change is a result of loss of layering due to annealing and nanoparticle coalescence. Furthermore, the reflectivity of the assembly annealed at higher temperature falls off faster with increasing Q than the one for the lower annealing temperature, which results from an increased surface and interface roughness.

To quantify these trends, we have fitted the data to multilayer models of the electron density. The results of these fits are shown by the dashed lines in Fig. 7, and it is apparent that these models describe the data quite well. Figure 8 shows the electron densities from these models. For the as-deposited assembly, the three layers are readily evident as regions of larger mass density than the PEI between the nanoparticle layers. These data demonstrate the layering associated with the nanoparticle assembly. The spacings between the first-second and second-third layers are both 6.5 nm. Annealing results in a dramatic reduction of the total assembly thickness (from 20 nm to between 6 and 10 nm), which results from the nanoparticle coalescence and modification of the PEI. As expected, concomitant with this is an increase in the layer electron density (Fig. 8), since FePt is conserved. Note the increase in width between the Si/assembly interface (near $z=0$) in the 800° C annealed assembly. This is likely a result of the initial stages of a reaction between the FePt and Si, which probably causes the reduction in the magnetic moment density for samples annealed at high temperatures. In over annealed assemblies, we have observed reaction of the FePt to form silicides.

7. Conclusions

We have studied 3 layer assemblies of FePt nanoparticles deposited by polymer-mediated self-assembly and annealed at various temperatures. For the as-deposited assembly the three layers are well distinguished. The Fe in the as-deposited assembly is significantly oxidized, the moment density of the assembly is small compared to bulk FePt, and the assembly shows no chemical order and no coercivity at room temperature. Annealing at increased temperatures leads to the onset of chemical order and an increase of the magnetic moment density that peaks at an annealing temperature of 650° C and reaches a value close to that of bulk FePt (normalized to the particle volume). The assemblies are ferromagnetic at room temperature for annealing temperatures of 580° C and above. With increasing annealing temperature the chemical order and coercivity increase, the Fe is less and less oxidized, but we also observe increased agglomeration and the layers are not well distinguished anymore. At very high annealing temperature the magnetic moment density drops possibly caused by chemical reactions with the Si substrate. Coercivities up to of 22.7 kOe were observed for the highest annealing temperature of 800°C. In order for these nanoparticles to form a basis of a successful magnetic recording medium it will be necessary to find process parameters that lead to ferromagnetic materials without the occurrence of severe agglomeration. Possible pathways are the addition of other elements such as Zr and Cu that have been shown to lead a reduction of the onset temperature for chemical order for thin film FePt [32].

Acknowledgements:

This research was carried out in part at the National Synchrotron Light Source, Brookhaven National Laboratory, which is supported by the U.S. Department of Energy, Division of Materials Sciences and Division of Chemical Sciences, under Contract No. DE-AC02-98CH10886, and in part at the Advanced Light Source, supported by the Office of Basic Energy Sciences, U.S. Department of Energy, under contract # DE-AC03-76SF00098.

References

- [1] Z. Zhang et al., IEEE Trans. Magn. **38**, 1861 (2002).
- [2] K. Stoev, F. Liu, Y. Chen, X. Dang, P. Luo, J. Chen, K. Kung, M. Lederman, M. Re, G. Choe, and M. Zheng, 47th Int. Conf. Magnetism and Magnetic Materials, Tampa, Florida 2002, paper AG-08.
- [3] R. Wood, IEEE Trans. Magn. **36**, 36 (2000).
- [4] D. Weller and A. Moser, IEEE Trans. Magn. **35**, 4423 (1999).
- [5] S. Sun, C. B. Murray, D. Weller, L. Folks, and A. Moser, Science **287**, 1989 (2000).
- [6] S. Sun, E. E. Fullerton, D. Weller, and C. B. Murray, IEEE Trans. Magn. **37**, 1239 (2001).
- [7] S. Sun, S. Anders, H. Hamann, J.-U. Thiele, J. E. E. Baglin, T. Thomson, E. E. Fullerton, C. B. Murray, and B. D. Terris, J. Am. Chem. Soc. **124**, 2884 (2002).
- [8] J. W. Harrell, S. Wang, D. E. Nikles, and M. Chen, Appl. Phys. Lett. **79**, 4393 (2001).
- [9] B. Stahl, N. S. Gajbhiye, G. Wilde, D. Kramer, J. Ellrich, M. Ghafari, H. Hahn, H. Gleiter, J. Weißmüller, R. Würschum, and P. Schlossmacher, Adv. Mater. **14**, 24 (2002).
- [10] S. Anders, S. Sun, C. B. Murray, C. T. Rettner, M. E. Best, T. Thomson, M. Albrecht, J.-U. Thiele, E. E. Fullerton, and B. D. Terris, Microelectr. Engin. **61/62**, 569 (2002).
- [11] D. Weller, A. Moser, L. Folks, M.E. Best, W. Lee, M. Toney, M. Schwieckert, J.-U. Thiele, and M.F. Doerner, IEEE Trans. Magn. **36**, 10 (2000)

- [12] R.F.C. Farrow, P.M. Rice, M.F. Toney, R.F. Marks, J. Hedstrom, and R. Stephenson, *J. Appl. Phys.*, submitted.
- [13] T. J. Regan, H. Ohldag, C. Stamm, F. Nolting, J. Lüning, J. Stöhr, and R. L. White, *Phys. Rev. B* **64**, 214422 (2001).
- [14] H.-J. Kim, J.-H. Park, and E. Vescovo, *Phys. Rev. B* **61**, 15284 (2000).
- [15] B. T. Thole and G. van der Laan, *Phys. Rev. B* **38**, 3158 (1988).
- [16] P. Kuiper, B. G. Searle, L.-C. Duda, R. M. Worf, and P. J. van der Zaag, *J. Electr. Spectrosc. Relat. Phenom.* **86**, 107 (1997).
- [17] P. Kuiper, B. G. Searle, P. Rudolf, L. H. Tjeng, and C. T. Chen, *Phys. Rev. Lett.* **70**, 1549 (1993).
- [18] J. H. Paterson and O. L. Krivanek, *Ultramicroscopy* **32**, 319 (1990).
- [19] A. R. B. de Castro, P. T. Fonseca, J. G. Pacheco, J. C. V. da Silva, E. G. L. da Silva, and M. H. A. Santana, *J. Magn. Magn. Mater.* **233**, 71 (2001).
- [20] A. R. B. Castro, R. D. Zysler, M. Vasquez Mansilla, C. Arciprete, and M. Dimitrijewits, *J. Magn. Magn. Mater.* **231**, 287 (2001).
- [21] F. Schedin, P. Morrall, V. N. Petrov, S. Case, M. F. Thomas, E. Dudzik, G. van der Laan, and G. Thornton, *J. Magn. Magn. Mater.* **211**, 266 (2000).
- [22] J. P. Crocombette, M. Pollak, F. Jollet, N. Thromat, and M. Gautier-Soyer, *Phys. Rev. B* **52**, 3143 (1995).
- [23] S. Gota, M. Gautier-Soyer, and M. Sacchi, *Phys. Rev. B* **62**, 4187 (2000).
- [24] S. Banerjee, S. Roy, J. W. Chen, and D. Chakravorty, *J. Magn. Magn. Mater.* **219**, 45 (2000).
- [25] J. Stöhr, *NEXAFS Spectroscopy*, Springer, Berlin 1992.

- [26] B. L. Henke, E. M. Gullikson, and J. C. Davis, *At. Data Nucl. Data Tables* **54**,181 (1993).
- [27] S. Gota, M. Gautier-Soyer, and M. Sacchi, *Phys. Rev. B* **62**, 4187 (2000).
- [28] R. Nakajima, J. Stöhr, and Y. U. Idzerda, *Phys. Rev. B* **59**, 6421 (1999).
- [29] A. Cebollada, R. F. C. Farrow, M. F. Toney, in *Magnetic Nanostructures*, Ed. H. S. Nalva, American Scientific Publishers, **2002**, pp93.
- [30] H. P. Alexander and L. E. Klug, *X-Ray diffraction Procedures for Polycrystalline and Amorphous Materials*, John Wiley & Sons: New York, 1962, BE Warren, *X-ray Diffraction*, Dover, New York, 1969
- [31] V. Holy, U. Pietsch, and T. Baumbach, in *High-Resolution X-ray Scattering from Thin Films and Multilayers*, Springer-Verlag, Berlin, 1998
- [32] S.-R. Lee, S. Yang, Y. K. Kim, and J. G. Na, *Appl. Phys. Lett.* **78**, 4001 (2001).

Captions for Figures

Figure 1: Magnetic moment density and coercivity as a function of anneal temperature for the FePt nanoparticle assemblies annealed in N₂.

Figure 2: Fe L edge absorption spectra of reference samples for metallic Fe and various oxides. The spectra are offset for clarity.

Figure 3: Fe L edge absorption spectra of 3 layer 4 nm FePt nanoparticle assemblies in the as-deposited state and after annealing at various temperatures. The spectra are offset for clarity.

Figure 4: Geometry for the estimation of the contribution to NEXAFS spectra stemming from a metallic FePt core and a surrounding iron oxide shell for a nanoparticle embedded in a carbonaceous matrix. The thicknesses of the carbonaceous layer, the first oxide layer, the metallic layer, and the second oxide layer for a give radial distance r from the nanoparticle center are given by z_C , z_{Ox1} , z_{FePt} , and z_{Ox2} .

Figure 5: In-plane X-ray diffraction of 3-layer Fe₅₈Pt₄₂ assemblies. The ordinate is the scattering vector Q , which is the difference between incident and diffracted X-rays. It has magnitude $Q = (4\pi/\lambda) \sin \theta$, where λ is the X-ray wavelength (about 0.12 nm here) and θ is half the scattering angle. The diffraction peaks are marked.

Figure 6: Annealing temperature dependence of average chemical order S_{ave} and chemically ordered fraction f_0 , and X-ray diffraction grain size d for the 3 layer assemblies.

Figure 7: X-ray reflectivity spectra for the 3 layer, 4 nm FePt assemblies for the as-deposited assembly (offset by a factor of 100) and the assemblies annealed at 580° C (offset by a factor of 3) and annealed at 800° C. Data are shown in the solid lines, while best fits are shown by the dashed lines.

Figure 8: Electron density profile deduced from the best fits to the reflectivity data in figure 7 for the as-deposited assembly and assemblies annealed at 580°C and 800° C. The position from the silicon substrate is z and $z=0$ is denotes the substrate surface.

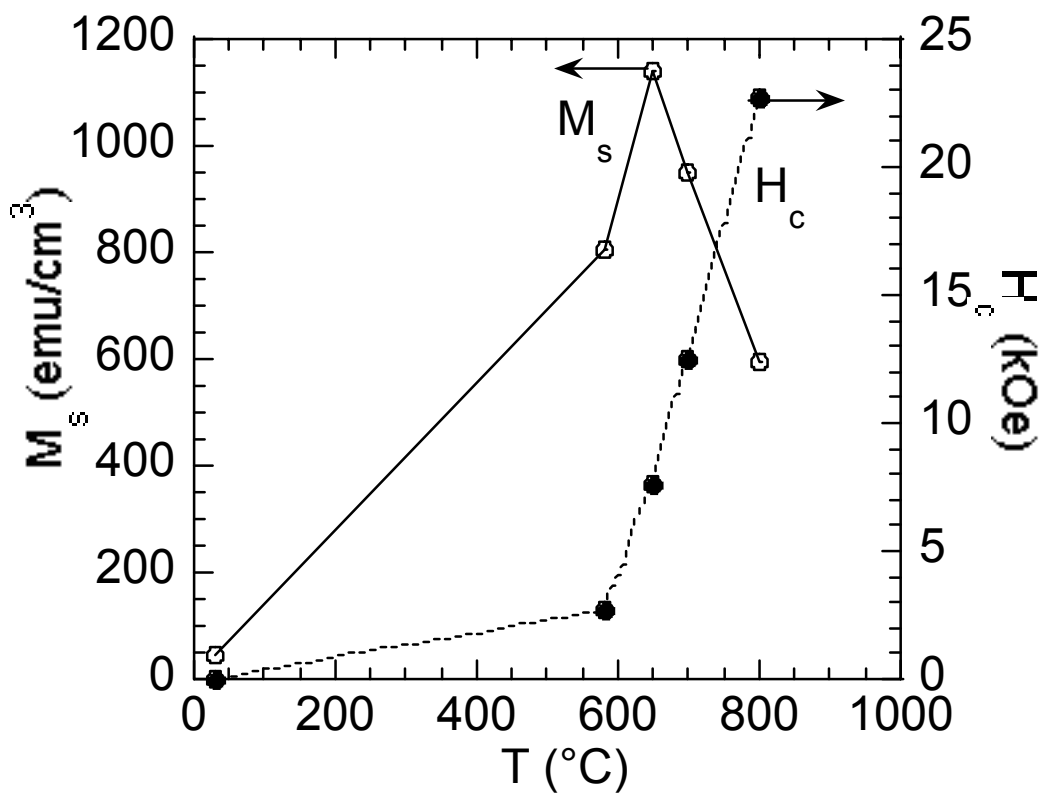


Figure 1

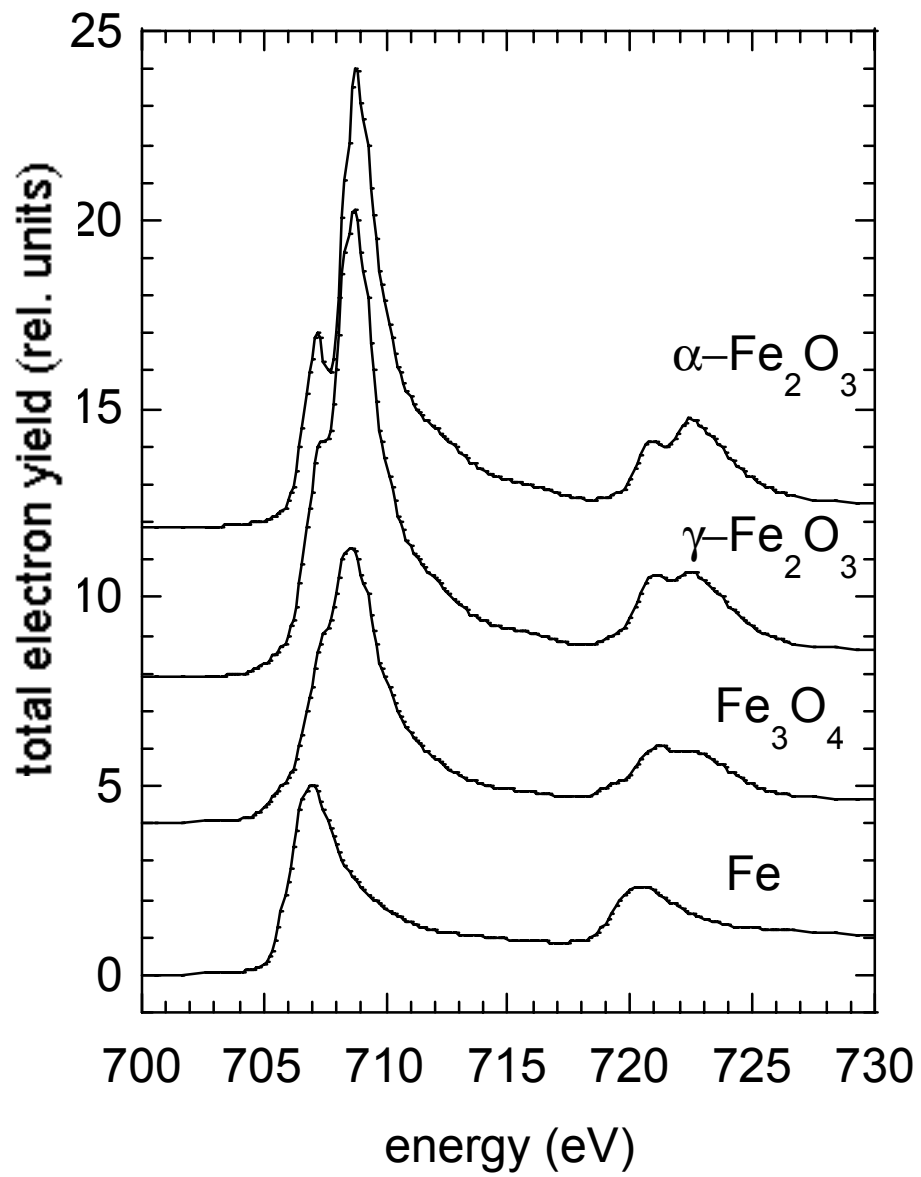


Figure 2

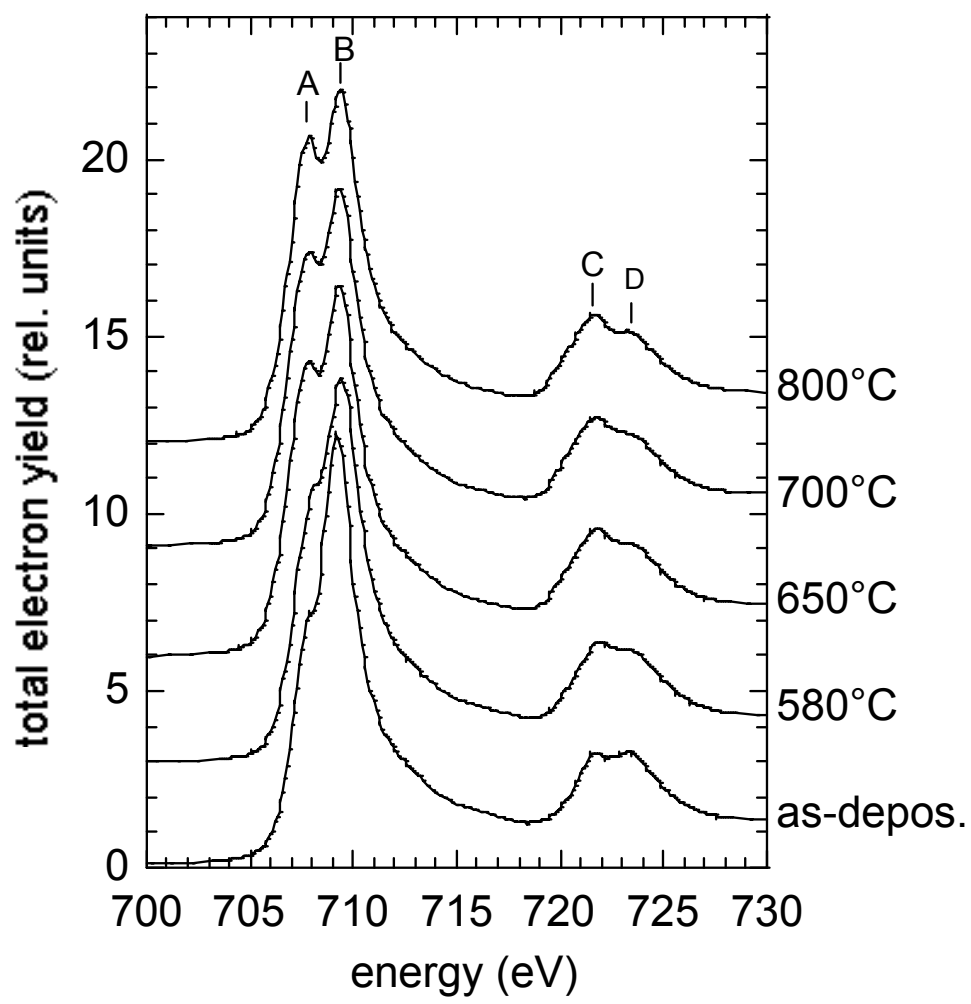


Figure 3

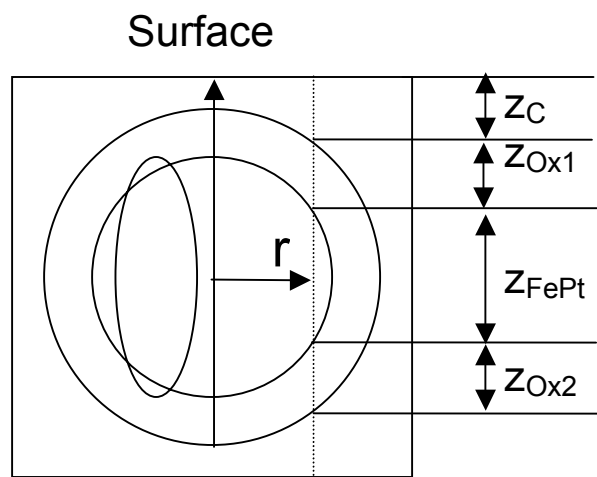


Figure 4

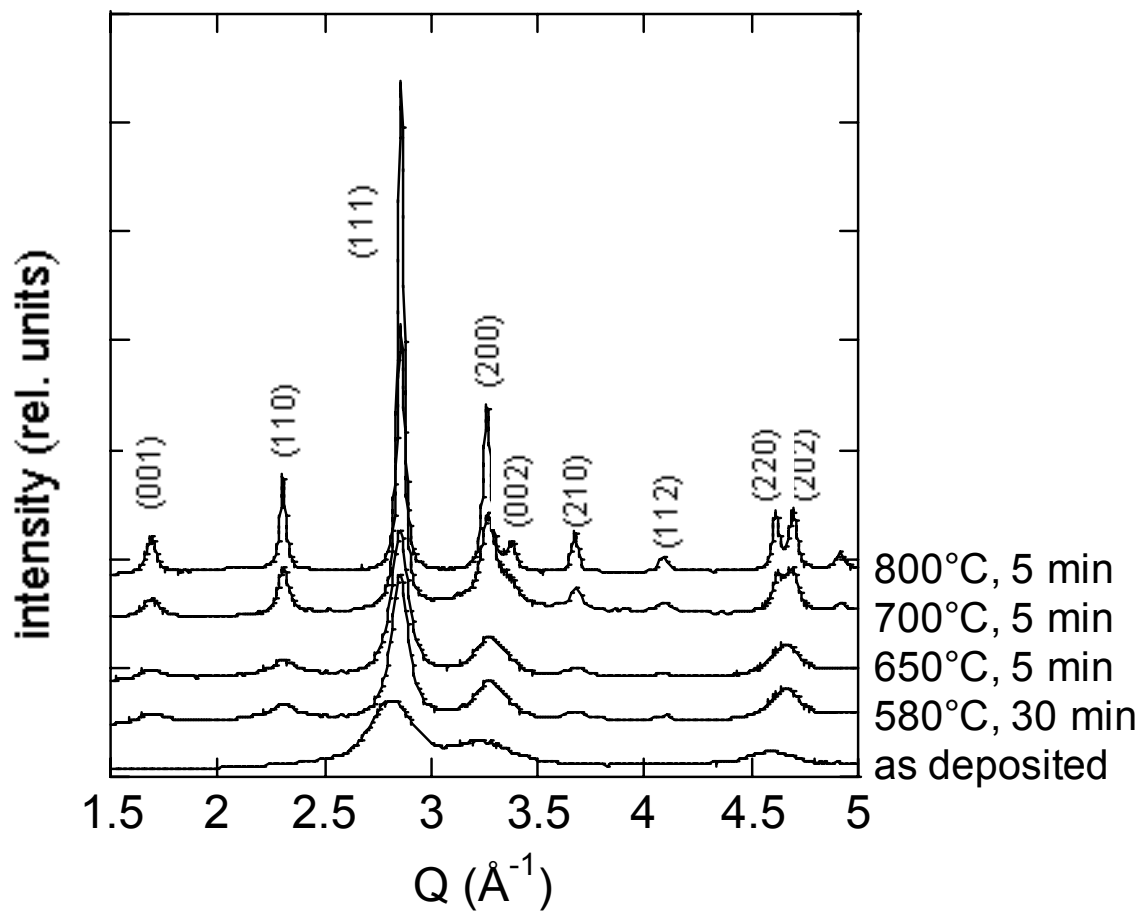


Figure 5

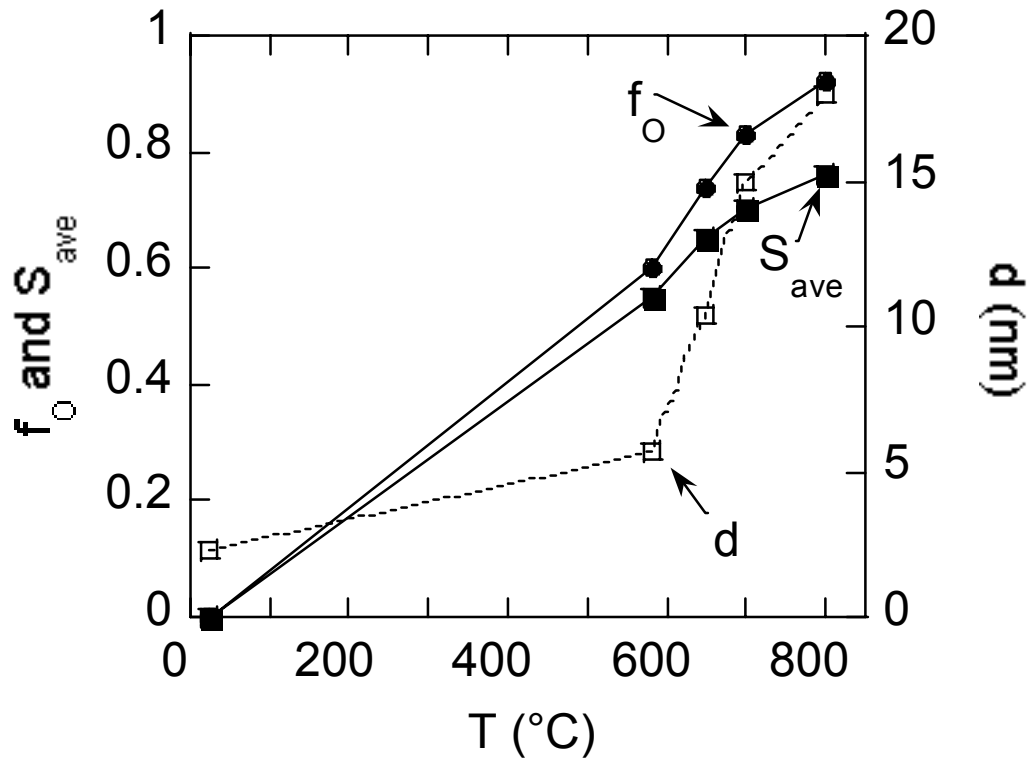


Figure 6

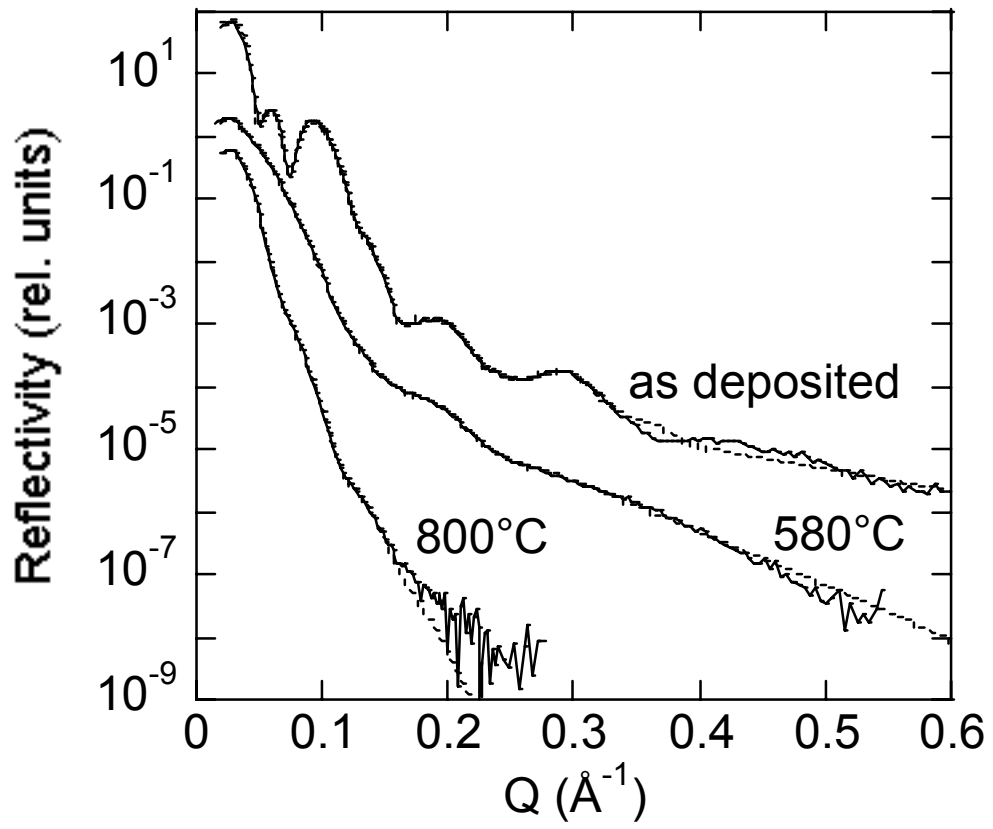


Figure 7

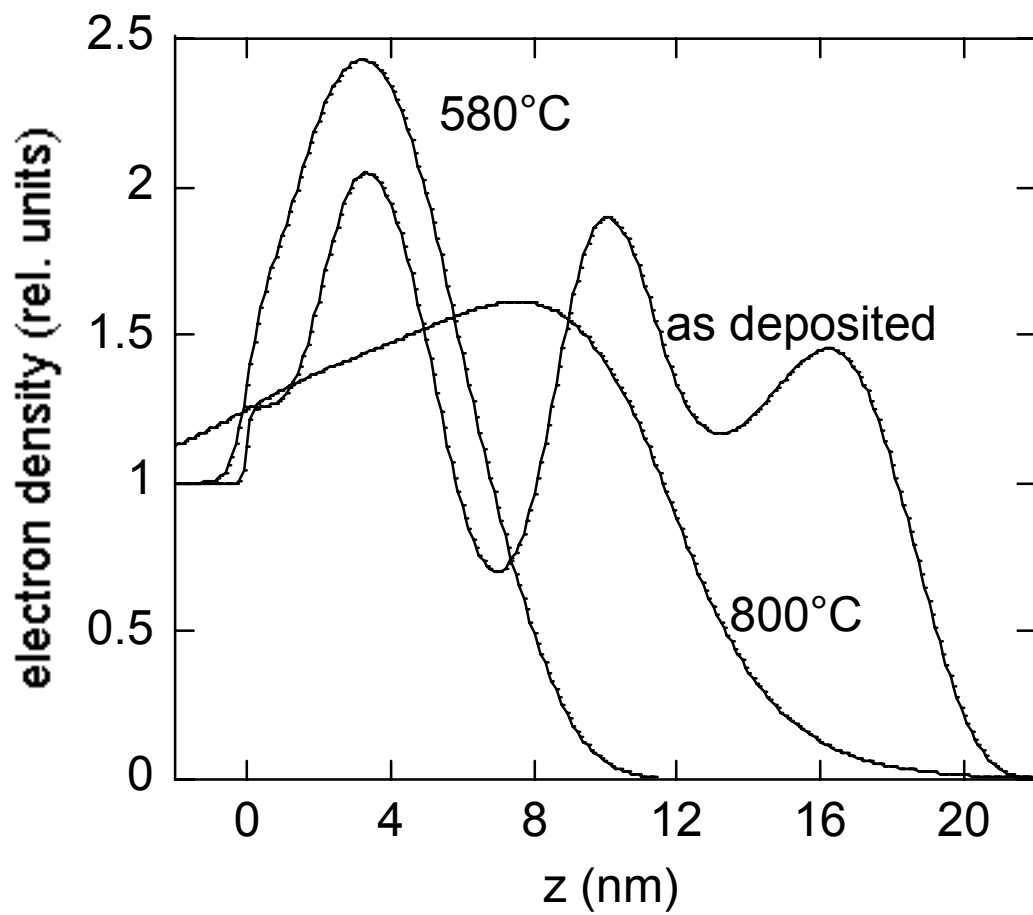


Figure 8